Int. J. Electrochem. Sci., 16 **(2021)** 150959, doi: 10.20964/2021.01.20

International Journal of
ELECTROCHEMICAL
SCIENCE
www.electrochemsci.org

Short Communication

Simulation and Experimental Research on Electrochemical Machining of Cross Groove

Hua Lin[1,2], *Yuanlong Chen*[1], *Xiang Li*[1], *Huigui Li*[1], *Qi Chen*[1,*]

[1] School of Mechanical Engineering, Hefei University of Technology, Hefei 230009, China
[2] School of Mechanical and Automotive Engineering, West Anhui University, Lu'an 237000, China
[*]E-mail: qichen@hfut.edu.cn

Received: 14 September 2020 / *Accepted:* 27 October 2020 / *Published:* 30 November 2020

The cross groove and its array structure are widely used in the aviation industry and the friction surface texture. Due to its unique advantages, the electrochemical machining (ECM) has broad prospects in the processing of special-shaped holes and grooves. In this work, the planar ECM of a single cross groove was taken as the object, and a cathode with an internal waist-shaped cross groove structure was designed. Further, and a three-dimensional multi-physics field coupling model was established based on the turbulent bubble flow model by coupling the model of an electric field and fluid heat transfer. The model was used to solve and analyze the bubble rate, temperature, and current density distribution in the machining equilibrium state. Thereafter, the orthogonal experiments were carried out, and the results were obtained. From the results, it was observed the groove contour quality was good, the machining process was stable, and the applied voltage and feed speed had significantly influenced the machining accuracy. Finally, the experiment produced a cross groove with an average entrance width of 2.66 mm and a bottom width of 2.35 mm.

Keywords: Cross groove; Electrochemical machining; Turbulent bubble flow; Multi-physical field coupling

1. INTRODUCTION

Micro-structures such as special-shaped grooves and holes are widely used in aviation, aerospace, weapons, and other equipment, such as cooling holes on engines, damping holes, grilles of stealth aircraft, and workpiece friction surface texture. Micro-structures are complex and mostly manufactured using refractory metal. They are usually manufactured using Electrical Discharge Machining (EDM), laser and Electrochemical Machining (ECM), etc [1-3].

ECM is a manufacturing technology in which material is removed based on the principle of electrochemical anode dissolution. Due to its unique manufacturing advantages, it has been successfully applied in the manufacturing process of special-shaped holes and grooves. Based on the advancement of the computer-based multi-physical coupling simulation technology, simulation has been widely used in ECM which significantly shortens the development cycle [4-7].

Fang et al. [8, 9] established a blade multi-physical field coupling temperature model, based on the time average quasi-steady-state algorithm, and used the sequential coupling method to solve the high-frequency pulse ECM temperature model. Chen et al. [10] conducted a multi-physical field coupling study based on the SST and Euler two-fluid model and compared the temperature field and contour changes when different physical fields were included. Deconinck et al. [11, 12] studied the changing process of metal ions in ECM based on the laminar flow and the multi-ion transport model. Klocke et al. [13] established a model for the ECM material removal process of the aero-engine parts. Fujisawa et al. [14] established a multi-physics model and predicted the ECM process.

Many researchers simplified the object into a two-dimensional model, generate bubbles based on different models, and use an indirect coupling to conduct the multi-physics coupling simulation research. However, there is no report on the multi-field full-coupling simulation of three-dimensional models. Therefore, it is of great significance to carry out the multi-field full coupling study of the three-dimensional model in order to improve the precision of the ECM.

Many researchers have studied the ECM process on groove structures. Zhao et al. [15] designed a hollow sheet cathode structure with stiffeners at different angles and conducted the fluid-solid coupling analysis and the flow field analysis. Further, they used the vibration feed mode for the process, and finally, a deep and narrow groove structure with a length to width ratio of 11:1, and depth to width ratio of 9:1 was fabricated. Wang et al. [16] used the electrochemical machining to process a deep and narrow groove structure with a groove width ranging from 2.73 mm to 2.78 mm on the surface of TB6. He et al. [17] established a multi-physics coupling model for the ECM for machining square holes in titanium alloy and discussed the influence of different process parameters on the hole quality. Zhang et al. [18] researched on the ECM process for machining of diamond-shaped holes, and the results showed that the cathode with a short arc through-hole flow channel had a the better flow field uniformity, and the side gap was between 0.2 mm and 0.25 mm.

Presently, the research on the ECM of a groove has achieved certain results. However, there are only a few researches on the ECM of the cross groove and the multi-field coupling simulation. In this work, the tool cathode structure was designed for the ECM process of machining a plane cross groove, and the three-dimensional multi-field coupling simulation model was established based on the turbulent bubble flow. Further, the fully coupled transient solution and the analysis are performed. The self-designed machining tooling was used for ECM experiments, which provided the theoretical and empirical support for studying the precision ECM of the cross grooves.

2. PRINCIPLE OF THE CROSS GROOVE ECM

Figure 1 shows the schematic diagram of the ECM principle of the cross groove. In this work, the length of the cross groove on the workpiece was greater than 10 mm and the width was lesser than 3 mm. Due to the particularity of its structure, the tooling structure was complicated in conditions such as when the reverse flow type was used, and when the flow field in the machining gap was extremely uneven when the side flow type was used to process the grooves. Therefore, in this work, the forward flow processing which is commonly used in the ECM of the slots and holes was adopted. In the forward flow ECM of the groove, the internal structure of the cathode is usually obtained using the method of biasing the theoretical contour inward. Further, in order to obtain a more uniform flow field in the machining gap, the waist-shaped cross groove was adopted in the cathode internal instead of the rectangular shaped cross groove. Moreover, and the internal groove size should be as large as possible.

Zhao and Lv et al. [15] designed a cathode with a waist-shaped internal hole for the ECM of the single straight and curved groove. The length and the width of the cathode were 30 mm and 2 mm respectively, and the width of the internal groove was 0.6 mm. Fang et al. [19] pointed out that increasing the size of the cathode internal hole in the ECM can improve the uniformity of the flow field and the processing stability. Therefore, in this work, the groove width was chosen to be 1.6 mm in this paper, and the center distance between the two semicircular holes was taken as 8 mm. The cathode structure and its related dimensions are shown in Figure 1.

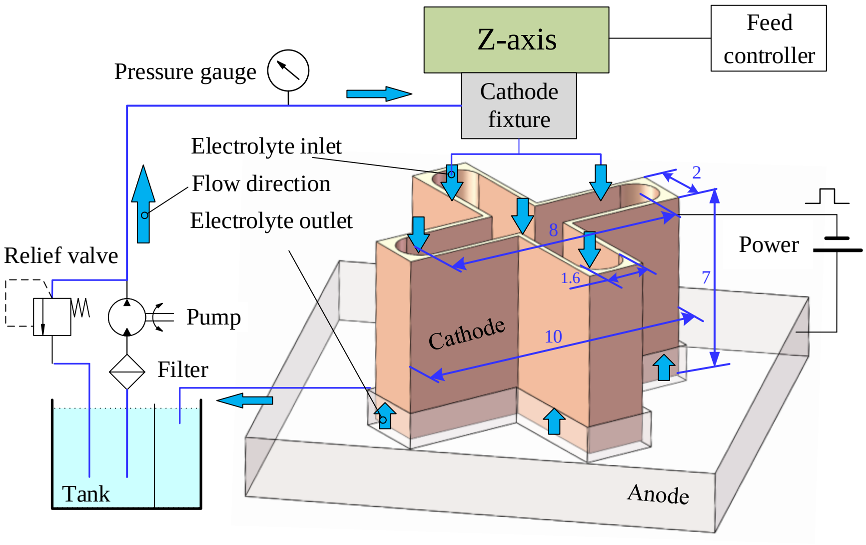

Figure 1. Schematic diagram of the ECM of a cross groove.

As shown in Figure 1, the electrolyte was pumped out of the electrolyte pool and passed through the filter. Further, is was flow into the cathode through the pipe and entered the machining gap between the cathode and the workpiece. Then it flew out from the machining side gap, and finally flew to the electrolyte cell. The tool cathode and the workpiece anode were applied with a processing voltage provided using a pulse power supply. The cathode was installed on the cathode fixture, and the cathode fixture was installed on the Z axis of the machine tool. Further, under the action of the feed controller, the tool cathode was fed linearly to the workpiece until the predetermined feed depth, and then returned to the origin of the machine tool.

While designing, tool cathodes of different structures also can be designed for various experiments, by changing the structure or the size of the hole or groove, and by changing the surface profile of the cathode outlet.

3. SIMULATION MODEL AND ANALYSIS

The derivation of the geometrical model, the electric field model, and the thermal model is briefly described below.

3.1 The geometric model

In this study, due to the symmetry of the cathode structure, and in order to reduce the calculation cost of the simulation, it was assumed that the machining is in equilibrium, and the four corners of the cross groove have the same forming law and they do not affect each other. This was assumed in order to consider a single corner of the cross groove as the research object, and then the half of a single corner was taken, and thereafter the one-eighth of the three-dimensional geometric model was established as shown in Figure 2(a). After the model was solved, the simulation results were symmetrically operated in order to obtain the entire cross groove ECM simulation results.

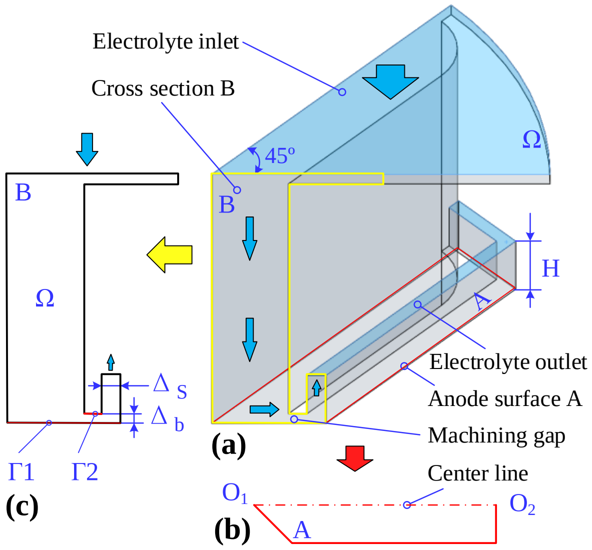

Figure 2. The geometric model of cross groove ECM. (a) The one-eighth of the flow model; (b) The anode surface; (c) The electric field boundary

In the Figure 2(a), the upper, lower, and bottom surface is the electrolyte inlet, electrolyte outlet, and the machining gap respectively, while Ω is the electrolyte area. In Figure 2(b), the anode surface in the model is denoted as A, the centerline is denoted as O_1O_2, where, O_1 is the origin. Further, the O_1O_2 direction is the positive direction, and its length is 5.2 mm. The machining gap Δ_b and the side gap Δ_s

are both set to 0.2 mm, and the outlet height *H* is equal to the processing depth of 1 mm. Furthermore, the electric field boundary setting is shown in Figure 2(c).

3.2 The electric field model

As shown in Figure 2(c), Γ1 denotes the anode boundary of the workpiece, Γ2 denotes the cathode boundary of the tool.

The anode boundary: Γ1=*U*, The cathode boundary: Γ2=0, in equilibrium, the potential in the electrolyte satisfies,

$$\nabla \cdot (\kappa \nabla \phi) = 0 \tag{1}$$

Where, κ is the electrolyte conductivity, and ϕ is the electric potential.

Electrolyte inlet and outlet boundary: $\partial \phi / \partial n = 0$

In the ECM, the electrolyte conductivity will be affected by the electrolyte temperature and bubble rate, and its change law can be expressed by the following formula [8]:

$$\kappa(x) = \kappa_0 [1 + \xi (T(x) - T_0)][1 - \beta(x)]^n \tag{2}$$

Where, κ_0 and T_0 is the initial conductivity and temperature of the electrolyte; ξ is the temperature coefficient, taking 0.02; β is the bubble rate; *n* is the influence index of the bubble rate, taking *n*=2. The normal dissolution rate of the workpiece is:

$$v_a = \eta \omega i \tag{3}$$

Where, *i* denotes the current density, ω denotes the volume electrochemical equivalent. η denotes the current efficiency.

3.4 Gas-liquid two-phase flow model

Multiphase flow models are usually divided into the separate multiphase flow model and the dispersed multiphase flow model. Among them, the dispersed multiphase flow model usually has four models: the bubble flow model, the mixed model, the Euler-Euler model, and the Euler-Lagrangian model.

In the process of ECM, the electrolyte, and the hydrogen bubble generated by electrolysis, and the solid generated by anode dissolution form a three-phase mixture in the machining gap. Since the volume of the solid phase is relatively small, the flow field model in the gap can be simplified into a gas-liquid two-phase fluid model, in which, liquid is the continuous phase and gas is the dispersed phase. Fang et al [9] used bubble flow model to simulate the bubbles generated near the cathode. Zhou et al [10] used the Euler-Euler model to simulate the gas phase volume fraction in the electrolyte.

In this work, the turbulent bubble flow model in the dispersed multiphase flow model was used to solve and analyze the gas-liquid two-phase flow field. In order to improve the solving efficiency of the three-dimensional flow field model, the *k*-*ε* turbulent flow model and the auto wall treatment was used.

In the turbulent bubble flow model, the liquid phase momentum equation, continuity equation and gas phase transport equation are respectively:

$$\Phi_1\rho_1\frac{\partial u_1}{\partial t}+\Phi_1\rho_1 u_1\cdot\nabla u_1=-\nabla p+\nabla\cdot\left[\Phi_1(\mu_1+\mu_T)\left(\nabla u_1+\nabla u_1^{T}-\frac{2}{3}(\nabla\cdot u_1)\right)I\right]+\Phi_1\rho_1 g+F \quad (4)$$

$$\left(\Phi_1\rho_1+\Phi_{\mathrm{g}}\rho_{\mathrm{g}}\right)+\nabla\cdot\left(\Phi_1\rho_1 u_1+\Phi_{\mathrm{g}}\rho_{\mathrm{g}} u_g\right)=0 \quad (5)$$

$$\frac{\partial\Phi_{\mathrm{g}}\rho_{\mathrm{g}}}{\partial t}+\nabla\cdot\left(\Phi_{\mathrm{g}}\rho_{\mathrm{g}} u_g\right)=-m_{\mathrm{g}1} \quad (6)$$

In which, the subscripts l and g represent the liquid and gas phases, u_l and u_g represent the velocity of the liquid and gas phases, ρ_l and ρ_g represent the density of the liquid and gas phases, Φ_l and Φ_g represent the volume fraction of the liquid and gas phases, *F* represent the any additional volume force, m_{gl} represent the mass transfer rate from the liquid to the gas phase.

When the flow field is turbulent, the bubble flow is similar to the single-phase turbulence model [20]. The turbulent source phase S_k generated by bubbles is introduced into equation *k* and Equation *ε*, and which is:

$$S_k=-C_k\Phi_{\mathrm{g}}\nabla p_2\cdot u_{\mathrm{slip}} \quad (7)$$

The velocity of gas in bubble flow and turbulent viscosity can be obtained:

$$u_g=u_1+u_{\mathrm{slip}}-\mu_1\frac{\nabla\Phi_g}{\rho_1\Phi_g} \quad (8)$$

$$\mu_{\mathrm{T}}=\rho_1 C_\mu\frac{k^2}{\varepsilon} \quad (9)$$

When $0.01<C_k<1$, $1<C_\varepsilon<1.92$, the simulation results are in good agreement with the experimental results [21]. The relationship between hydrogen mass flux generated by cathode and local current density in ECM is:

$$N_{H2}=\mathrm{M}\frac{\eta i}{2\mathrm{F}} \quad (10)$$

Where, N_{H2} is hydrogen flux, M is molar mass of hydrogen, η is current efficiency, regardless of oxygen generation, take η=1. The model constants of turbulent bubble flow are shown in Table 1.

Table 1. The turbulent bubble flow model simulation parameters.

$C_{1\varepsilon}$	$C_{2\varepsilon}$	C_μ	C_ε	C_k	σ_k	σ_ε
1.44	1.92	0.09	1.46	0.505	1	1.3

3.5 Thermal model

In the processing of ECM, the heat is mainly composed of the Joule heat of the electrolyte and the electrochemical reaction heat at the electrode boundary of the electrolyte. The resistance of tool cathode and workpiece anode is very small, so the Joule heat generated during the process of ECM can be ignored. Thus, the electrolyte temperature distribution in the gap can be described by the convection-diffusion equation of the fluid [10].

$$\rho c_p\frac{\partial T}{\partial t}+\rho c_p u_1\cdot\nabla T=\nabla\cdot(k_t\nabla T)+Q_{\mathrm{bulk}} \quad (11)$$

$$Q_{\text{bulk}} = Q_j + Q_r \tag{12}$$

$$Q_j = \kappa(\nabla U)^2 \tag{13}$$

$$Q_r = U_k i_k \tag{14}$$

Where, c_p is the specific heat capacity of electrolyte at atmospheric pressure, k_t is the thermal conductivity of electrolyte, Q_{bulk} is the heat generated during the ECM process, Q_j is the Joule heat, Q_r is the reaction heat at the boundary, U_k is the overpotential, i_k is the current density of the electrochemical boundary double layer.

3.6 Multi-physical field coupling analysis and simulation process

3.6.1 Multi-physical field coupling analysis

The coupling among the multi-physical fields in the ECM process is a strong coupling. After making relevant assumptions, the model can be transformed into a weakly coupled problem for indirect solving, or can be solved directly in a fully coupled way.

In the simulation work, the volume flux can be set in the turbulent bubble flow module to couple the electric field to generate bubbles. The convection term in the convection diffusion equation for fluid heat transfer is used to couple the effect of the flow field velocity on heat transfer. The heat source term is set to couple the electric field to generate Joule heat and the electrochemical boundary reaction heat. The conductivity equation of the electrolyte material domain is set to couple the relationship between the gas-liquid two-phase flow field, the electric field and the fluid heat transfer.

In this work, it was assumed that the processing of ECM was entered the equilibrium state, and the anode geometric domain changed during the cathode feed were not considered. The solution was carried out by the fully coupled direct transient solution method.

3.6.2 The simulation process

The process of the multi-physical field coupling simulation solution of the cross groove ECM is shown in Figure 3.

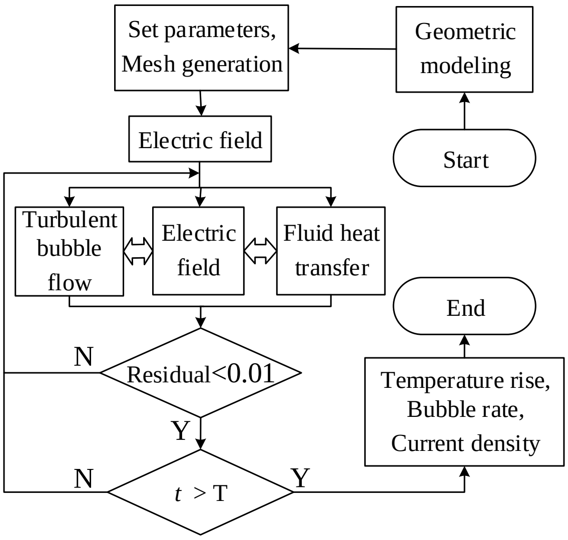

Figure 3. Flow chart of multi-physical field coupling simulation solution.

In Figure 3, the 3D geometric model was imported into the multi-physics simulation software *COMSOL Multiphysics* for solution. Then the turbulent bubble flow, electric field (primary current), fluid heat transfer modules were added. After the boundary conditions and meshing were set, the electric field was solved in a steady state to obtain the initial distribution of the electric field. The result was transferred as the initial value to the turbulent bubble flow, fluid heat transfer and current field for transient simultaneous solving. Finally, the temperature, gas volume fraction and current density were obtained.

3.7 Simulation parameters

The relevant initial values and process parameter settings in the simulation model are shown in Table 2.

Table 2. Physical properties of anode, cathode and electrolyte.

Physical parameter	Value
Initial conductivity of electrolyte k_0/(S/m)	7.2
Electrolyte density ρ/(Kg/m^3)	1070
Specific heat capacity of electrolyte c_p/[J/(kg·K)]	3730
The initial temperature T_0/(K)	298.15
Entrance velocity v_i/(m/s)	0.3
Outlet pressure p_o/(MPa)	0
Hydrogen molar mass M_{H2}/(g/mol)	2
Bubble size /(×10^{-3}mm)	1
Applied voltage U/(V)	16
Processing time t /(s)	5

4. SIMULATION ANALYSIS AND RESULTS

During analysis, the simulation parameters were set and the analysis was carried out. The bubble rate, temperature, electrolyte conductivity in the machining gap and the current density distribution on the anode surface A are shown in Figure 4. The current density on the centerline O_1O_2 is shown in Figure 5.

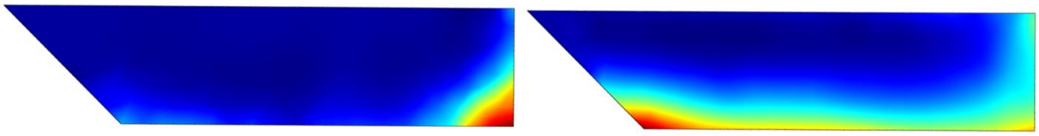

(a) Gas volume fraction (c) Electrolyte conductivity

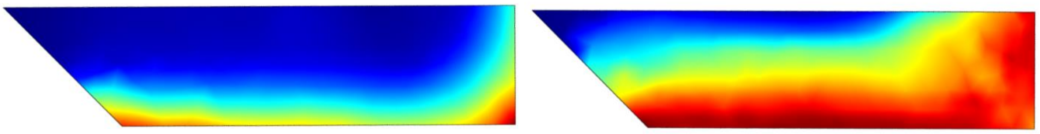

(b) Temperature rise (d) Current density

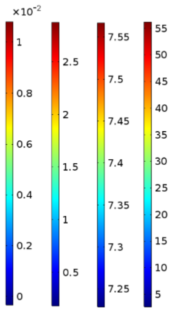

(a) (b) (c) (d)

Figure 4. The simulation results. (a) Gas volume fraction; (b) temperature rise distribution; (c) electrolyte conductivity; (d) current density on anode surface A.

From Figure 4(a), it is observed that the bubble rate on the anode surface A is very less which reaches the maximum value of about 1.1% at the exit of the edge, and it is almost zero at the centerline. This is due to the generation of the bubble near the cathode surface. Further, as the fluid flows to the side gap and the outlet, the amount of the diffusion to the anode surface is less. However, in the simulation, it was observed that the maximum bubble volume fraction near the cathode surface is about 18%. The similar results were shown in the study conducted by Zhou et al.[10], in which the bubble rate at the outlet was about 0.23 and the outlet was set with backpressure. Moreover, the electrode length was taken as 50mm.

Since the flow velocity in the bottom gap and the side gap reached about 3~4 m/s, the higher flow velocity rapidly results in electrolysis products and heat out of the gap, and the temperature rise on the anode surface was not obvious. As shown in Figure 4(b), it is observed that the maximum temperature rise is only about 3 K.

Due to the combined effect of temperature rise and the hydrogen bubbles, it can be seen from Figure 4(c) that the maximum electrolyte conductivity on the anode surface is about 7.57 S/m, which is an increase of 5.1% from the initial value of 7.2 S/m (Figure 4(c)). Further, there is almost no change at the centerline.

From Figure 4(d), it is observed that the current density distribution in the machining gap is uneven due to the uneven distribution of the electrical conductivity. It is also found that the current density value on the entire anode surface ranges from 3.4 A/cm^2 to 55.3 A/cm^2, with a large range of variation.

The current density on O_1O_2 of the anode surface A is shown in Figure 5. From Figure 5, it is observed that the current density value at the centerline 0~4 mm is very less and reaches the maximum value near the edge of the cathode, and gradually decreases in the side gap. This is because the dissolution degree of the anode surface is proportional to the current density and the current efficiency. Therefore, the dissolution values on the anode surface are uneven.

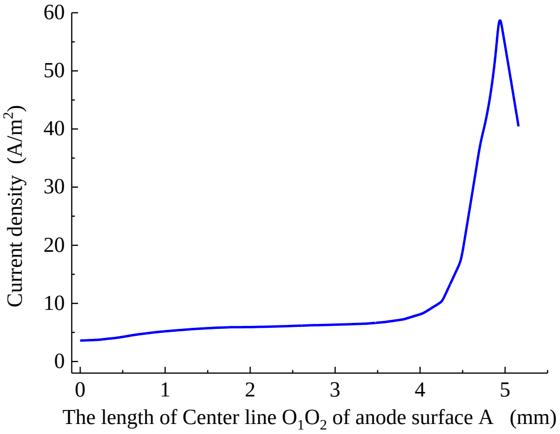

Figure 5. The current density on the centerline O_1O_2 of the anode surface A.

5. ECM EXPERIMENT AND RESULT ANALYSIS

The experiment preparation, parameter, and design of the experiment and the results of the orthogonal experiment and analysis are described below.

5.1 Experiment preparation

In order to further study and analyze the influence of the processing parameters of the ECM of the cross groove, based on the laboratory's ECM experiment system, the tooling fixture was designed and tested. The front and rear views of the cathode that was used for the experiment is shown in Figure 6(a) and Figure 6(b), and the experimental device is shown in Figure 6(c). The cathode was made using a CNC machining center. The material of the cathode and the cathode fixture was brass, and the workpiece was a SS304 plate.

As shown in Figure 6(c), the workpiece was fixed on the worktable of the ECM machine tool. The cathode, the cathode fixture, the connecting block and the Z-axis of the machine tool were fixed together. Further, a pressure gauge was installed at the entrance of the tooling fixture in order to observe the pressure of the electrolyte, and these parts were well sealed in order to prevent the leakage of the electrolyte.

(a) Front view of cathode (b) Rear view of cathode

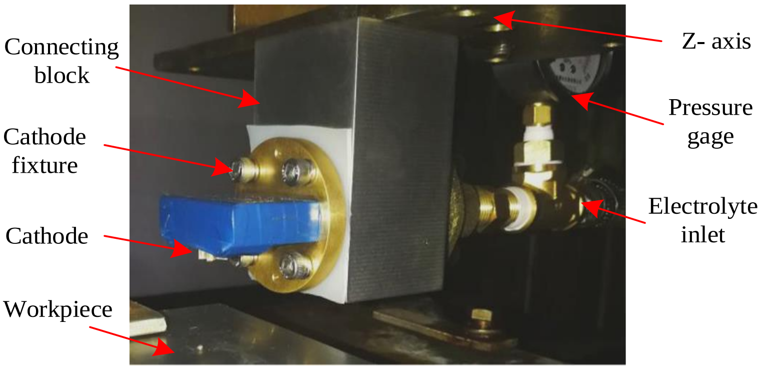

(c) Experimental device

Figure 6. Photographs of the cathode and the experimental device.

5.2 Parameters and design of experiment

The process parameter values that were used in the cross groove ECM experiment are shown in Table 3. The pulse power frequency was 40 kHz and the duty cycle can be adjusted. In Table 3, The pressure data refers to gauge pressure. The electrolyte used in the experiment was 8 wt% $NaNO_3$, the initial temperature was 298.15 K, and the conductivity was 7.2 S/m.

Table 3. Main parameters of cross groove machining.

Parameter	value
Peak voltage U/(V)	16~24
Duty cycle	0.8
Inlet pressure P_i/(MPa)	0.01~0.03
Outlet pressure P_o/(MPa)	0
Feed velocity v_c/(mm/min)	0.1~0.4
Processing depth H_a/(mm)	1
Initial machining gap Δ_0/(mm)	0.2~0.5

In order to study the influence of the parameters on the machining accuracy and stability, the best combination of the processing parameters for the ECM of the cross grooves was obtained. The design of the orthogonal experiment method was adopted using the orthogonal array, and the interaction of different factors was not considered. In this study, the four-factor three-level orthogonal table L_9 (3^4) was selected, and four factors such as processing applied voltage, feed speed, electrolyte pressure and the initial machining gap were used as factors A, B, C and D. Each of the factors is designed with 3 levels as shown in Table 4.

Table 4. Orthogonal experimental factors and levels.

Processing Parameters	Peak voltage /V	Feed velocity /mm/min	Electrolyte pressure /MPa	Initial machining gap /mm
Factor	A	B	C	D
Level 1	16	0.2	0.01	0.5
Level 2	20	0.3	0.02	0.35
Level 3	24	0.4	0.03	0.2

5.3 Orthogonal experiment results and discussions

5.3.1 Experiment evaluation

After the ECM, the average entrance and bottom width of the cross grooves were measured. The position of each measurement point is shown in Figure 7. The width values of the entrance and the bottom are represented by B_{ix} and B_{ox}, and x is ranged from 1 to 12, each corner takes three points, each separated by 1mm. The average width of the entrance and bottom of the cross grooves values were denoted as B_i and B_o.

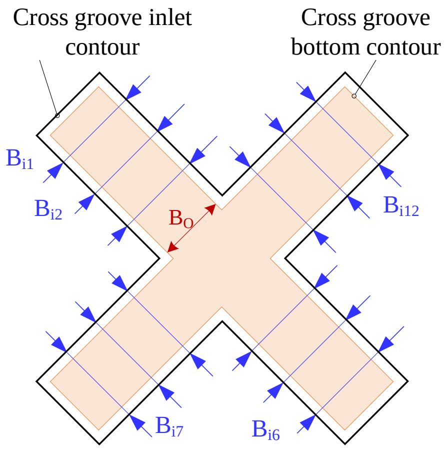

Figure 7. Schematic diagram of cross groove width measurement.

5.3.2 Orthogonal experiment results and discussions

The orthogonal experiment was carried out in 9 combinations. The width values are shown in Table 5. Based on the experiment results observed in Table 5, the range analysis and variance analysis were performed. The order of influence on the entrance width of the cross groove was: A-B-C-D, and the range values were 0.211, 0.186, 0.181 and 0.107 respectively. The root mean square values were: 0.078, 0.039, 0.026, and 0.01 respectively. Further, the order of the influence on the bottom width was: A-B-C-D, and the range values were 0.183, 0.083, 0.083, and 0.03, respectively. Moreover, the root mean square values were: 0.026, 0.006, 0.005 and 0.001.

According to the trend chart of factors and indicators, it was found that a better combination of process conditions is obtained using $A_1B_3C_3D_2$.

Table 5. Orthogonal experimental results.

	A	B	C	D	B_i (mm)	B_O (mm)
1	1(16)	1(0.2)	1(0.1)	1(0.5)	2.94	2.49
2	1	2(0.3)	2(0.2)	2(0.35)	2.73	2.43
3	1	3(0.4)	3(0.3)	3(0.2)	2.66	2.35
4	2(20)	1	2	3	2.94	2.54
5	2	2	3	1	2.71	2.45
6	2	3	1	2	2.77	2.48
7	3(24)	1	3	2	2.95	2.59
8	3	2	1	3	3.17	2.68
9	3	3	2	1	2.84	2.54

The average entrance and the bottom width of the cross groove during the optimized experiment were 2.64 mm and 2.46 mm respectively. Moreover, the result of width was very close to the result of the $A_1B_3C_3D_3$, however, the taper of the optimized groove wall was less. The photos of the cross grooves that were processed under the combination parameter of $A_1B_3C_3D_3$ and $A_1B_3C_3D_2$ are shown in Figure 8(a) and Figure 8(b). The photographs that were taken with a microscope camera (Minmei Microscope Camera M50) are shown in Figure 8(c).

In this work, the cross groove width and the side gap were similar to the results of Zhao's study [15]. In his study, the linear feed and vibration feed were adopted, the straight groove entrance width was ranged from 2.45 mm to 2.55 mm, the entrance side gap after the processing of ECM was about 0.2 mm~0.3 mm [15-18,22].

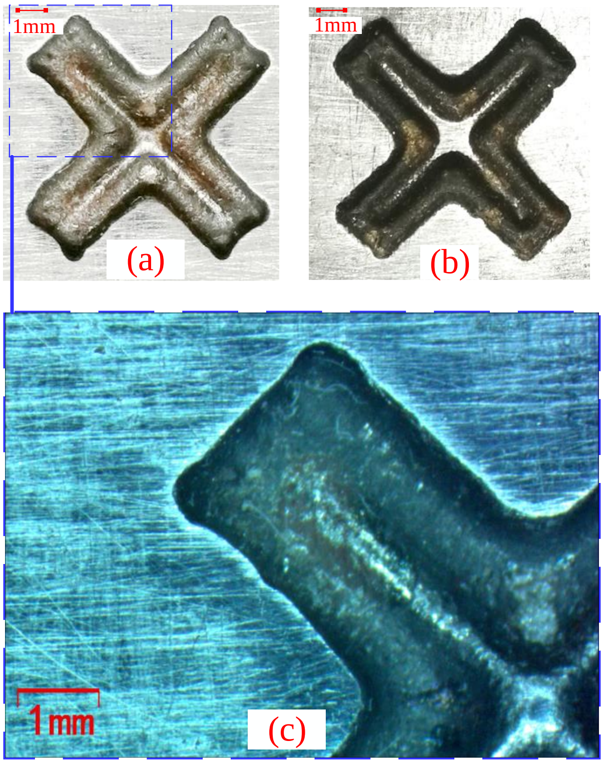

Figure 8. Cross groove photos after ECM. (a) $A_1B_3C_3D_3$; (b) $A_1B_3C_3D_2$; (c) A photograph taken by a microscope camera

From Figure 8(a), it is observed that the groove dissolves relatively more at each of the corners, so that the contour shapes near each corner have certain fluctuations. In Figure 8(b), the convex structure in the middle of the workpiece is more obvious. The reason is that, during the ECM processing, the initial machining gap was bigger, and the anode surface receives a relatively smaller current density. Therefore, the less dissolution is obtained at the center. Further, a reasonable adjustment of processing parameters was found to achieve the purpose of improving the accuracy of the cross grooves. Moreover, when adjusting the process parameters, small gap processing should be adopted, and priority should be given to reducing the average voltage and increasing the feed velocity.

Furthermore, it is noted that the convex structures in the middle of the cross grooves in the experiment are of different sizes. This phenomenon is also closely related to the cathode structure and the processing parameters.

6. CONCLUSIONS

In this work, a three-dimensional multi-physical field coupling model for the ECM of cross grooves based on turbulent bubble flow was established and was coupled with the electric field and the fluid heat transfer. Thereafter it was solved using a transient full coupling method. The simulation results showed that the bubble rate on the anode surface was only about 1%, the temperature rise was 3 K. Further, the electrolyte conductivity increased by about 5%, and the current density on the anode surface was extremely uneven. The orthogonal experiment results of the ECM of cross grooves showed that the machining process was stable and it was observed that the grooves had better contour shapes. Moreover, when the processing parameters such as the peak voltage, feed rate, electrolyte inlet pressure, and initial machining gap were 16 V, 0.4 mm/min, 0.03 MPa, and 0.2 mm respectively, the width of the entrance groove was 2.66 mm and the bottom width was 2.35 mm. Among the processing parameters, the average voltage and the feed speed had a significant influence on the groove width.

Furthermore, it was found that the main reason for the convex structure at the center of the cross groove is attributed to the uneven current density.

ACKNOWLEDGEMENTS
This study has been funded by the National Natural Science Foundation of China (No. 51775161 and 51775158), hereby gratefully acknowledged.

References

1. K.P. Rajurkar, G. Levy, A. Malshe, M. M. Sundaram, J. McGeough, X. Hu, R. Resnick and A. DeSilva, *CIRP Annals,* 55 (2006) 643.
2. K. P. Rajurkar, M. M. Sundaram and A. P. Malshe, *Procedia CIRP,* 6 (2013) 13.
3. C. F. Zhang, H. H. Ai, Z. H. Yan, X. G. Jiang, P. Y. Cheng, H. Tian and Y. W. Hu, *Int. J. Electrochem. Sci.,* 15 (2020) 3453.
4. A. A. Nayak, S. Gangopadhyay and D. K. Sahoo, *J. Manuf. Processes,* 23 (2016) 269.
5. S. K. Rathore and M. K. Das, *Int. J. Heat Mass Transfer,* 95 (2016) 636.
6. M. H. Wang, W. S. Liu and W. Peng, *Int. J. Adv. Manuf. Technol.*, 74 (2014) 749.
7. Z. Y. Xu, L. Y. Sun, Y. Hu and J. C. Zhang, *Int. J. Adv. Manuf. Technol.*, 71 (2014) 459.
8. Y. L. Chen, M. Fang and L. J. Jiang, *Int. J. Adv. Manuf. Technol.*, 91 (2017) 2455.
9. M. Fang, Y. L. Chen, L. J. Jiang, Y. S. Su and Y. Liang,. *Int. J. Adv. Manuf. Technol.*, 105 (2019) 3261.
10. Y. L. Chen, X. C. Zhou, P. X Chen and Z. Q. Wang, *Chinese. J. Aeronaut.*, 33 (2020) 1057.
11. D. Deconinck, S. Van Damme and J. Deconinck, *Electrochim. Acta*, 69 (2012) 120.
12. D. Deconinck, S. Van Damme and J. Deconinck, *Electrochim. Acta*, 60 (2012) 321.
13. F. Klocke, M. Zeis, S. Harst, A. Klink, D. Veselovac and M. Baumgärtner, *Procedia CIRP,* 8 (2013) 265.
14. T. Fujisawa, K. Inaba, M. Yamamoto and D. Kato, *J. Fluid Eng.*, 130 (2008).
15. J. S. Zhao, Y. M. Lv, F. Wang, and Y. F. He, *Int. J. Adv. Manuf. Technol.*, 96 (2018) 2245.
16. F. Wang, J. S. Zhao, Y. M. Lv, Z. W. Yang and Z. J. Tian, *Int. J. Adv. Manuf. Technol.*, 92 (2017) 3063.
17. Y. He, H. Xiao, W. Gan, Q. Yu and F. Yin, *Procedia CIRP,* 68 (2018) 751.
18. J. S. Zhao, F. Wang, X. L. Zhang, Z. W. Yang and Y. F. He, *Procedia CIRP,* 68 (2018) 684.
19. X. L. Fang, N. S. Qu, H. S. Li and D. Zhu, *Journal of South China University of Technology(Natural Sicence Edition), 41* (2013) 137. (In Chinese)
20. S. Becker, A. Sokolichin and G. Eigenberger, *Chem. Eng.*, 49 (1994) 5747.
21. D. Kuzmin, and S. Turek, *In 3rd International Symposium on Two-Phase Flow Modelling and Experimentation,* 9 (2004) 22.
22. F. Wang, J. S. Zhao, D. M. Liu, Y. T. Fan and Z. J. Tian, *Int. J. Electrochem. Sci.,* 13 (2018) 9466